

IV. SUMMARY AND CONCLUSION

The results presented in this paper suggest that whitening can be used to improve EMG amplitude estimation for FES (and other systems that require epoch-based estimates). The improvement, evaluated via EMGamp-torque estimation errors, when going from single-channel unwhitened to multiple-channel whitened estimates was approximately 22%. Generally, half of this improvement was due to whitening, while the other half was attributed to the use of multiple-channel EMG. Furthermore, computing whitened single-channel estimates yielded roughly the same results as multiple-channel estimates without whitening. This result is consistent with the work presented in [8]. It is important to note that torque estimation was used as a proxy for EMG amplitude estimation, and a one-to-one relationship between them does not exist. For instance, even if the processing techniques provided perfect estimates of EMG amplitude, the resulting torque estimation error would not be 0% due to model inaccuracies and measurement errors. Thus, the percentage reductions in torque errors due to whitening and multiple channels likely underestimate the improvement in EMG amplitude estimator performance.

For the combined noise rejection/adaptive whitening filter, orders between 12 and 18 yielded both the lowest average error in estimated torque and the highest percentage of whitened estimates being an improvement over unwhitened estimates. The optimal order for the whitening filter also stays between 12 and 18 at each of the three epoch durations. The epoch-based algorithms presented in this paper were an improvement over the stream-based algorithms in terms of average error, optimal filter length, and filter length consistency. Filter design via the least-squares design technique might also be useful in stream-based algorithms when lower filter orders are beneficial (e.g., to reduce computational load in real-time applications). In summary, our best epoch-based, multiple-channel, adaptive whitening algorithm produced 21.4%–22.5% less error than the unwhitened single-channel technique in an EMGamp-torque estimation task.

REFERENCES

- [1] K. Englehart and B. Hudgins, "A robust, real-time control scheme for multifunction myoelectric control," *IEEE Trans. Biomed. Eng.*, vol. 50, no. 7, pp. 848–854, Jul. 2003.
- [2] G. L. Gottlieb and G. C. Agarwal, "Dynamic relationship between isometric muscle tension and the electromyogram in man," *J. Appl. Physiol.*, vol. 30, pp. 345–351, 1971.
- [3] E. A. Clancy, S. Bouchard, and D. Rancourt, "Estimation and application of EMG amplitude during dynamic contractions," *IEEE Eng. Med. Biol. Mag.*, vol. 20, no. 6, pp. 47–54, Nov.–Dec. 2001.
- [4] P. Bonato, T. D'Alessio, and M. Knaflitz, "A statistical method for the measurement of muscle activation intervals from surface myoelectric signal during gait," *IEEE Trans. Biomed. Eng.*, vol. 45, no. 3, pp. 287–299, Mar. 1998.
- [5] J. P. Giuffrida and P. E. Crago, "Reciprocal EMG control of elbow extension by FES," *IEEE Trans. Neural Syst. Rehab. Eng.*, vol. 9, no. 4, pp. 338–345, Dec. 2001.
- [6] R. Thorsen, R. Spadone, and M. Ferrarin, "A pilot study of myoelectrically controlled FES of upper extremity," *IEEE Trans. Neural Syst. Rehab. Eng.*, vol. 9, no. 2, pp. 161–168, Jun. 2001.
- [7] N. Hogan and R. W. Mann, "Myoelectric signal processing: Optimal estimation applied to electromyography-part II: Experimental demonstration of optimal myo-processor performance," *IEEE Trans. Biomed. Eng.*, vol. BME-27, pp. 396–410, 1980.
- [8] E. A. Clancy and K. A. Farry, "Adaptive whitening of the electromyogram to improve amplitude estimation," *IEEE Trans. Biomed. Eng.*, vol. 47, no. 6, pp. 709–719, Jun. 2000.
- [9] M. I. A. Harba and P. A. Lynn, "Optimizing the acquisition and processing of surface electromyographic signals," *J. Biomed. Eng.*, vol. BME-3, pp. 100–106, 1981.

- [10] E. Kaiser and I. Petersen, "Adaptive filter for EMG control signals," in *The Control of Upper-Extremity Prostheses and Orthoses*, P. Herberts, R. Kadefors, R. Magnusson, and I. Peterson, Eds. Springfield, IL: Charles C. Thomas, 1974, pp. 54–57.
- [11] Y. St-Amant, D. Rancourt, and E. A. Clancy, "Influence of smoothing window length on electromyogram amplitude estimates," *IEEE Trans. Biomed. Eng.*, vol. 45, no. 6, pp. 795–799, Jun. 1998.
- [12] E. A. Clancy, E. L. Morin, and R. Merletti, "Sampling, noise-reduction and amplitude estimation issues in surface electromyography," *J. Electromyogr. Kinesiol.*, vol. 12, pp. 1–16, 2002.
- [13] J. G. Proakis and D. G. Manolakis, *Digital Signal Processing Principles, Algorithms, and Application*. Upper Saddle River, NJ: Prentice-Hall, 1996, pp. 623, 701–630, 724.
- [14] C. A. Salini, J. A. Tranquilli, and P. Prakash, "Adaptive whitening in electromyogram amplitude estimation for epoch-based applications," Worcester Polytech. Inst., Dept. Elect. Comput. Eng., Worcester, MA, Dec. 16, 2003. Major Qualifying Project Report.

Analytical Model of Extracellular Potentials in a Tissue Slab With a Finite Bath

Joseph V. Tranquillo, Dana O. Burwell, and Craig S. Henriquez*

Abstract—Extracellular potentials are often used to assess the activation and repolarization of transmembrane action potentials in cardiac tissue under a variety of experimental conditions. An analytical model of the extracellular potentials arising from a planar wavefront propagating in a three-dimensional slab of cardiac tissue with a variably thick adjacent volume conductor or bath is presented. Starting with the transmembrane potential, the model yields the extracellular potentials at various points in the bath and inside tissue. The results show that the analytical model produces signal timecourses with trivial computational costs that are similar to those computed from a full reaction-diffusion bidomain model with different bath thicknesses for tissue with uniform properties and for tissue with an abrupt ionic inhomogeneity.

Index Terms—Bidomain, cardiac electrophysiology, extracellular potentials.

I. INTRODUCTION

Extracellular potentials (ϕ_e) are often used to determine the time of cellular activation during propagation and, thus, provide spatial maps of the activation wavefront. In some situations, the signals are also used to access local and spatial changes in refractoriness, possibly revealing an arrhythmogenic substrate. Because the extracellular potential is the result of current sources throughout the tissue, it depends on many factors, including the timecourse of the transmembrane potential, the relative locations of the sensing and reference electrodes, the electrical conductivities of the intracellular and interstitial spaces and the size of the adjacent volume conductor. Numerically solving the full reaction-diffusion bidomain equations that govern cardiac current flow in three dimensions can require considerable computational resources.

Manuscript received January 25, 2004; revised July 2, 2004. This work was supported in part by National Science Foundation (NSF) under Grant DBI-9974533. *Astertisk indicates corresponding author.*

J. V. Tranquillo and D. O. Burwell are with the Department of Biomedical Engineering, Duke University, Durham, NC 27708 USA.

*C. S. Henriquez is with the Department of Biomedical Engineering, 136 Hudson Hall, P.O. Box 90281, Duke University, Durham NC 27708-0281 USA (e-mail: ch@duke.edu).

Digital Object Identifier 10.1109/TBME.2004.840467

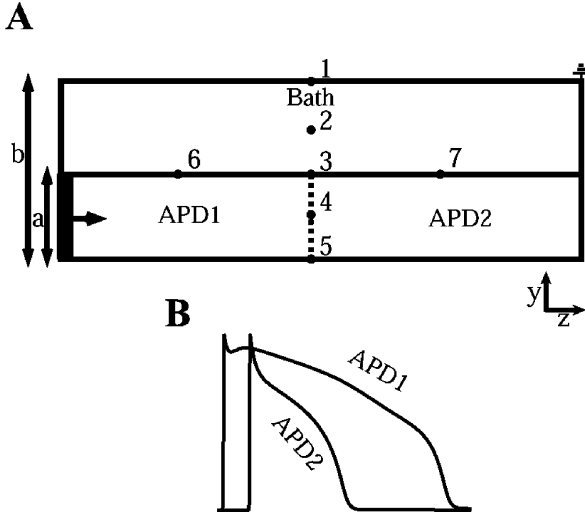


Fig. 1. (A) Geometry of a 3-D slab of finite thickness (a) surrounded by variably thick (b) volume conductor. A planar wave front propagates along the z axis, causing every yz cross section to be the same. Potentials were recorded at the center of the domain at $y = b$ for site 1, $y = (b + a)/2$ for site 2, $y = a$ for site 3, $y = a/2$ for site 4 and $y = 0$ for site 5. Sites 6 and 7 are located on the tissue surface 1 cm from site 3. (B) Long (APD1) and short (APD2) action potential time courses used in the simulations. The short action potential is used for the entire tissue domain in all initial simulations.

Analytic models, on the other hand, are typically computationally inexpensive and provide additional insight into the relationship between the transmembrane potential and extracellular potential. The classical models were developed for tissue with either an infinite [1] or absent volume conductor (i.e., only interstitial space) [2]. In many practical experimental and clinical situations, however, the volume conductor or adjoining bath has a finite extent and the shape of the recorded extracellular potential differs from that expected from these classical models, leading to a possible misinterpretation of the signal timecourse.

In this paper, we develop an analytical model of the potentials arising from a planar wavefront propagating in a three-dimensional (3-D) slab of cardiac tissue with a variably thick adjacent volume conductor. Using a monodomain model to obtain the spatio-temporal transmembrane potential, the analytical model can be used to obtain the potentials at points in the bath and tissue for various bath thicknesses. The signals are compared with those computed from full reaction-diffusion bidomain models with equal anisotropy for tissue with uniform membrane properties and for tissue with an ionic inhomogeneity. The results show that the bath thickness markedly impacts the shape of the recorded signal. The results also show that the monodomain and analytical models together can be used to accurately predict the extracellular potentials of the bidomain model in both the bath and the tissue under a variety of experimentally relevant conditions and with smaller computational costs.

II. METHODS

We consider potentials (ϕ) in an infinitely extended planar tissue slab of thickness a [Fig. 1(A)] with an adjacent isotopic bath of finite thickness, $b - a$. The tissue slab is considered to be a bidomain in which the intracellular (i) and interstitial (e) domains are continuous and separated everywhere by a membrane. The adjoining volume conductor or bath is composed only of an extracellular space (o) that is contiguous with the interstitial space of the tissue. For simplicity we assume a uniform planar wavefront, eliminating variation in one dimension (x). Within the tissue the current fluxes are

$$\mathbf{J}_i = -\nabla \cdot (\mathbf{D}_i \nabla \phi_i), \quad \mathbf{J}_e = -\nabla \cdot (\mathbf{D}_e \nabla \phi_e) \quad (1)$$

where $\mathbf{D}_{i,e}$ are the intracellular and interstitial bidomain conductivity tensors and we assume that $\mathbf{D}_i = k\mathbf{D}_e$ (i.e., equal anisotropy). Since transmembrane current (I_m) flowing from one domain must pass through a membrane into the other domain

$$\nabla \cdot (\mathbf{J}_i + \mathbf{J}_e) = 0, \quad -\nabla \cdot \mathbf{J}_i = \nabla \cdot \mathbf{J}_e = I_m. \quad (2)$$

For simplicity of presentation, a partial derivation of the equations for ϕ_e and ϕ_i is given below. The derivation follows that of Henriquez *et al.* for a planar slab bidomain with an infinite bath [1], but with different boundary conditions to account for the finite bath extent.

The solutions for ϕ_e and ϕ_i are the sum of homogeneous (h) and particular (p) solutions, $\phi_e = \phi_e^h + \phi_e^p$ and $\phi_i = \phi_i^h + \phi_i^p$ where

$$\phi_e^p(y, z) = -\frac{g_{iz}}{g_{iz} + g_{ez}} V_m(z), \quad \phi_i^p(y, z) = \frac{g_{ez}}{g_{iz} + g_{ez}} V_m(z). \quad (3)$$

$V_m(z) = \phi_i - \phi_e$ and g_i and g_e are the scalar values of the intracellular and interstitial conductivity tensors ($\mathbf{D}_{i,e}$ in (1)) along the y and z axes. Furthermore, $\phi_e^h = \phi_i^h = \phi^h$. The homogeneous (ϕ^h) and bath (ϕ_o) potentials are solutions to Laplace's equation in Cartesian coordinates. At $y = 0$, symmetry requires that $\partial\phi_h/\partial y = 0$ [1]. At the tissue-bath interface ($y = a$), the interstitial and extracellular potentials are continuous and the interstitial current leaving the tissue along the y direction is equal to the extracellular current entering the bath. This implies that the intracellular current density vanishes at the tissue-bath surface. In contrast to the derivation of Henriquez *et al.*, an additional boundary condition must be imposed to deal with the finite bath extent. At the bath-air interface ($y = b$), no flux is assumed, namely

$$\sigma_o \frac{\partial\phi_o}{\partial y} \Big|_{y=b} = 0 \quad (4)$$

where σ_o is the extracellular (bath) conductivity. Using these boundary conditions and assuming equal anisotropy ($g_{iy}/g_{ey} = g_{iz}/g_{ez}$)

$$\phi_o(y, z) = \frac{-g_{iz}}{q} F^{-1} \{V_m(k) (H_1(y, k) + H_2(y, k))\} \quad (5)$$

$$\phi^h(y, z) = \sigma_o \frac{g_{iz}}{g_{iz} + g_{ez}} F^{-1} \{V_m(k) H_3(y, k)\} \quad (6)$$

such that

$$\begin{aligned} \phi_e(y, z) &= \phi^h(y, z) + \phi_e^p(y, z) \\ &= \sigma_o \frac{g_{iz}}{g_{iz} + g_{ez}} F^{-1} \{V_m(k) H_3(y, k)\} - \frac{g_{iz}}{g_{iz} + g_{ez}} V_m(z) \end{aligned} \quad (7)$$

where F^{-1} is the inverse Fourier transform, $q = \sqrt{(g_{iz} + g_{ez})/(g_{iy} + g_{ey})}$ and the filter coefficients are given by

$$H_1(y, k) = \frac{\sinh(q|k|a)e^{-|k|y}}{\gamma - \xi} \quad (8)$$

$$H_2(y, k) = \frac{\sinh(q|k|a)e^{|k|(y-2b)}}{\gamma - \xi} \quad (9)$$

$$H_3(y, k) = \frac{(e^{-|k|a} - e^{|k|(a-2b)}) \cosh(q|k|y)}{\gamma - \xi} \quad (10)$$

$$\gamma = (e^{-|k|a} + e^{|k|(a-2b)})q(g_{ey} + g_{iy}) \sinh(q|k|a) \quad (11)$$

$$\xi = \sigma_o (e^{|k|(a-2b)} - e^{-|k|a}) \cosh(q|k|a). \quad (12)$$

$V_m(k)$ in (5) and (6) is the Fourier transform of $V_m(a, z)$. Unless otherwise noted, all potentials (ϕ), including V_m , are in the spatial domain (z). The form of $V_m(a, z)$ can be itself an analytic function or derived from a reaction diffusion model (see below).

The analytical (3) and (5)–(12) were implemented in a MATLAB script to arrive at general solutions for ϕ_e and ϕ_o . The Fourier transforms were evaluated using a fast Fourier transform algorithm [3]. To reduce ringing in the frequency domain, the spatial extent was $z = 25.0$ cm to support a full action potential in space (i.e., the action potential never leaves the domain). $V_m(z)$ was also offset such that the resting membrane potential was 0 mV.

In addition to the analytical model, extracellular potentials were numerically computed using a full reaction-diffusion bidomain

$$\begin{aligned} \nabla \cdot (\mathbf{D}_i + \mathbf{D}_e)\phi_e &= -\nabla \cdot (\mathbf{D}_i \nabla V_m) \\ \nabla \cdot (\mathbf{D}_i V_m) + \nabla \cdot (\mathbf{D}_i \nabla \phi_e) &= -\beta I_m \\ I_m &= C_m \frac{\partial V_m}{\partial t} + I_{ion} \end{aligned} \quad (13)$$

with a bounding bath. A computationally less expensive but less complete description of cardiac propagation is the monodomain model

$$\nabla \cdot (\mathbf{D}_{bulk} V_m) = -\beta I_m \quad (14)$$

where \mathbf{D}_{bulk} represents the bulk properties of the intracellular and interstitial spaces, can be derived from the bidomain model by assuming $\phi_e = 0$ mV everywhere or assuming equal anisotropy. Only one potential is solved for at each time step so the monodomain is less computationally intensive than the bidomain. The extracellular and interstitial potentials can be computed from the monodomain using either our analytical solution or a separate computational scheme. One common scheme for computing extracellular potentials is the monopole current source method

$$\phi_e = \frac{1}{4\pi\sigma_o} \int \frac{I_m}{r} dV \quad (15)$$

where I_m are the transmembrane current sources, dV are the volumes from which the current sources arise and r is the distance from the current sources to the recording electrode [4], [5]. For the numerical solution of (13) and (14), the coupling matrices for the intracellular and extracellular spaces ($\mathbf{D}_{i,e}$) were computed using a vertex centered finite volume method [6]. An in-house cardiac simulation system, Cardiovave, was used to integrate the bidomain equations with $\Delta t = 2 \mu\text{s}$ and $\beta = 2000 \text{ cm}^{-1}$.

Two methods can be used to obtain $V_m(a, z)$ for the analytic model. First, $V_m(a, z)$ can be supplied directly from the monodomain solutions. Because the wavefront is planar (i.e., no bath is present), only a one-dimensional (1-D) model is required. Another method of obtaining $V_m(a, z)$ is to use a precomputed action potential shape in time, $V_m(t)$, and assume uniform conduction along the z -axis. This approach will make the computation significantly faster as no reaction diffusion model is required. Under conditions where the spatial distribution of current flow can be affected by regional changes in membrane properties, a full reaction diffusion model may be required. For these studies we have chosen to compute $V_m(a, z)$ from a 1-D monodomain simulation. The Luo–Rudy dynamic model [7] was used in the simulations and was modified to produce the default action potentials, $V_m(t)$, with action potential durations (APDs) $\text{APD}_{90} = 100 \text{ ms}$ [APD2 in Fig. 1(B)], by halving the time constants τ_d and τ_f , and reducing the conductivity of the slow inward current to $g_{si} = 0.03 \text{ mS/cm}$.

Analytic and bidomain-derived solutions were found for a tissue ($a = 1.0 \text{ cm}$) that adjoins no bath ($b = a$), a thin bath ($b = a + 2.0 \text{ mm}$) or a thick bath ($b = a + 4.0 \text{ cm}$). In tissue with uniform membrane properties, the short action potential was used and the equally anisotropic conductivities were $g_{iz} = 5.0 \text{ mS/cm}$, $g_{ez} = 4.0 \text{ mS/cm}$, $g_{iy} = .5 \text{ mS/cm}$, $g_{ey} = .4 \text{ mS/cm}$. The bath conductivity was $\sigma_o = 6 \text{ mS/cm}$. To achieve the same wavespeed in the monodomain and bidomain solutions, bulk conductivities ($g_i g_e / (g_i + g_e)$) were

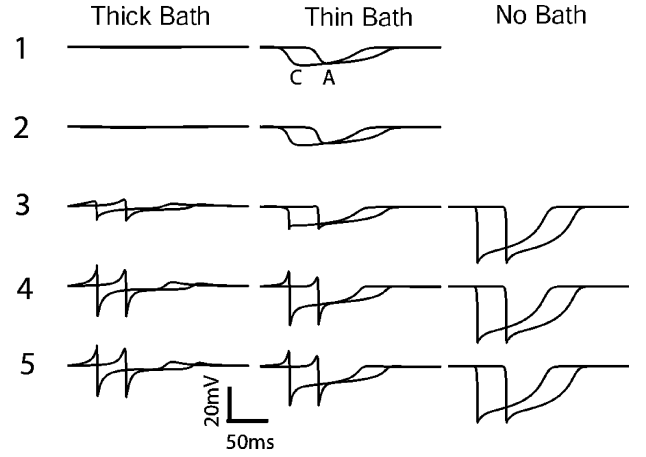


Fig. 2. Comparison of the analytic (A) and simulated (C) solutions for the thick, thin and no bath cases at sites 1–5. Note that all analytic potentials have been shifted in time by 35 ms and the short LR action potential was used everywhere in the tissue.

used for the monodomain model. Unipolar extracellular potentials were recorded at the center of the domain [Fig. 1(A)] from the top of the bath [$y = b$, site 1 in Fig. 1(A)], middle of the bath ($y = (b + a)/2$, site 2), tissue surface ($y = a$, site 3), middle of the tissue ($y = a/2$, site 4) and bottom of the tissue ($y = 0$, site 5). For bidomain and monodomain simulations, the spatial discretization was $\Delta x = \Delta y = \Delta z = 100 \mu\text{m}$. Since the bidomain equations do not have a unique solution, a ground point was fixed to 0 mV for all time and placed at the top of the bath opposite the stimulus. For no bath cases, the ground was placed at the top of the tissue opposite the stimulus. The ground locations and the extent of the tissue (z -axis) ensure that no active current sources approach the ground. This ground was also assumed to be a distant reference. The monodomain simulations do not require a ground because only the transmembrane potential (a difference between the intracellular and interstitial potential) is computed. The analytic solution also does not require a ground since the derivation assumes an infinite extent along the z -axis and as $z \rightarrow \infty$, all potentials approach 0 mV. The distant reference for the monodomain and analytic unipolar potential was taken in the far corner of the domain (i.e., same location as the ground for the bidomain simulations).

To study the effect of a spatial change in the APD (an ionic inhomogeneity), the same tissue domain was used but the action potential in half of the tissue along the z dimension was replaced with an action potential model with a longer APD of $\text{APD}_{90} = 244 \text{ ms}$ [APD1 in Fig. 1(B)] produced by increasing the slow inward conductance to $g_{si} = 0.09 \text{ mS/cm}$. Surface extracellular potentials ($y = a$) were solved at three points on the tissue surface (sites 6, 3, and 7 separated by 1 cm) with no bath, a thin bath and thick bath. In these simulations, a wavefront was initiated moving from the region of long APD to short APD. The $V_m(a, z)$ used in the analytical model was supplied from the monodomain simulation.

III. RESULTS

The extracellular potentials derived from the analytical model were compared to those obtained from reaction diffusion bidomain models for three cases: a large bath (4.0 cm), small bath (2.0 mm) and no bath. Extracellular potentials were computed at 2 sites in the bath [1 and 2 in Fig. 1(A) when present] and three sites in the tissue [3–5 in Fig. 1(A)]. Recall that all potentials were referenced to the ground (i.e., a point far from any activity) such that the signals are effectively unipolar. For the given parameters, the conduction velocity for all cases was 68 cm/s. Fig. 2 shows that the unipolar potentials obtained from the analytical

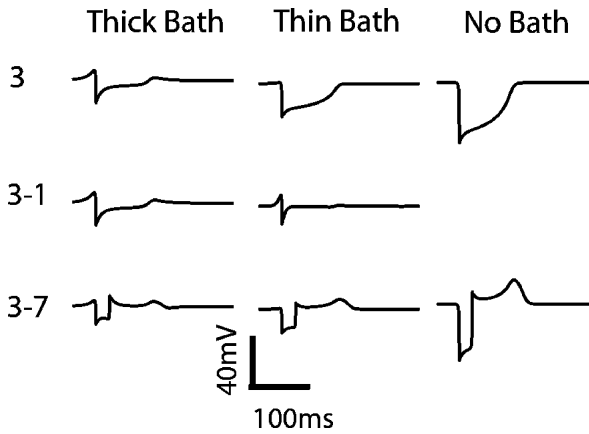


Fig. 3. The surface potential at site 3 referenced to the distant ground (3), site 1 (3-1), and site 7 (3-7) for the three cases.

solution are similar at all sites to those obtained using the full bidomain solution. Note that the two curves were offset 35 ms to improve visual comparison on the same axis. The shape of the signal depends on the location of the recording site. For the thick bath case, ϕ_e at the tissue surface (site 3) has a biphasic deflection corresponding to the arrival of the upstroke of the underlying $V_m(t)$. A secondary deflection (T-wave) corresponds to the repolarization of $V_m(t)$. For the 1.0-cm tissue thickness used, the potentials in the depth (sites 4 and 5) have a similar biphasic shape to those at the surface although with increased amplitude (peak-to-peak $\phi_e = 17.4$ mV at site 3, $\phi_e = 31.6$ mV at site 4 and $\phi_e = 33.0$ mV at site 5). Bath potentials within 2–3 mm of the tissue surface (not shown) are biphasic and reduced in amplitude but are nearly isopotential (0 mV) far from the surface (sites 1 and 2). It should be noted that reducing the bath thickness from 4 cm to approximately 0.5 cm does not change the amplitude or timecourse of surface potential (deviates less than 1%). A more significant reduction in the bath thickness, however, does change the timecourse, as exemplified by the thin bath case ($b = a + 2$ mm).

In the thin bath case, the surface potential (ϕ_e at site 3) is monophasic and resembles an inverted and scaled version of $V_m(t)$ [see (3)]. Potentials in the bath at sites 1 and 2 are also inverted monophasic signals and due to the close proximity to the tissue surface are only slightly smaller in amplitude than those at site 3. Potentials within the tissue (sites 4 and 5) are more biphasic because the surrounding tissue acts as an effective, symmetric volume conductor. In the no bath case, the potentials throughout the tissue are all inverted and monophasic as expected from core conductor theory [3].

The analytical model can be used to study signals where the reference electrode is moved closer to the recording electrode. Referencing a surface potential (site 3) to a bath potential (site 1) does not impact the shape of the signal for the thick bath case but does change the shape of the signal when the bath is thin (Fig. 3). With this electrode configuration, the recorded signal in the thin bath is biphasic (Fig. 3, 3-1). When the reference electrode for the thick bath case is moved to a distant site on the tissue (site 6 or 7), the bipolar signal is no longer biphasic but takes on a “U” shape. The “U” shape is maintained for this electrode configuration for the thin and no bath cases.

The analytical and bidomain models were also used to compute ϕ_e , for the three bath thicknesses, at three surface locations (6, 3, and 7) in the presence of an ionic inhomogeneity (AP1 has a long duration and AP2 has a short duration). In the thick bath case, as the wavefront passes from a long APD to a short APD, the polarity of the T-wave switches from negative (when the electrode is placed on the tissue with the long APD) to positive (when the electrode is placed on the tissue

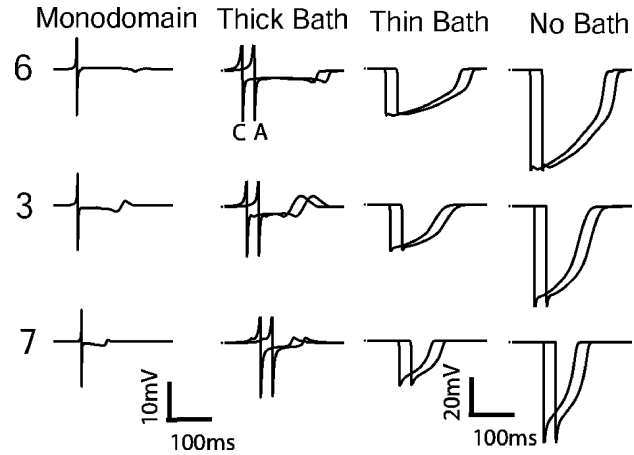


Fig. 4. Comparison of the analytic (A) and simulated (C) solutions for the monopolar current source approximation, thick bath, thin bath and no bath cases at three locations on the surface of the tissue in the presence of an ionic inhomogeneity. Note that all analytic potentials have been shifted in time by 35 ms and the short LR action potential was used everywhere in the tissue.

with the short APD). Still with regard to the large bath case, the extracellular potentials using the current source models [see (15)] are qualitatively similar to those obtained with the analytical and bidomain models. The relationship between the underlying $V_m(t)$ and ϕ_e , however, is preserved as well as the polarity of the T-wave. For the thin and no bath cases, however, the biphasic potentials from the current source model do not resemble the potentials predicted by the analytic and bidomain solutions, which are inverted monophasic signals at all three sites that follow the timecourse of the underlying $V_m(t)$ (Fig. 4). Thus, the temporal extent of ϕ_e in the analytic and bidomain models reflects the temporal extent of the underlying action potential.

While passing $V_m(z)$ from a monodomain to the analytic model has a small effect on the accuracy of ϕ_e , it is significantly faster and requires less memory than using the full reaction diffusion bidomain model. For example, the two-dimensional bidomain model with a thick bath (1.3 million nodes), required 12 hours and 784 MB of memory on 32 processors. In contrast, solving an equivalent 1-D monodomain (130 000 nodes with no bath) required 6 min and 0.5 MB on 32 processors. The computation of extracellular potential via $V_m(z)$ with the analytical model requires approximately 5 min on a single Pentium 1.3-GHz processor. Note that the analytical model can use a stylized action potential and activation times, making the overall computation of the extracellular potential trivial.

IV. DISCUSSION AND CONCLUSION

The analytical model of the extracellular potential developed in this paper has been shown to reproduce the timecourse of the potentials generated by a full reaction diffusion bidomain model under a variety of conditions but with significantly less computational overhead. The model predicts the extracellular timecourses for a variety of tissue preparations with both homogeneous and inhomogeneous properties with finite bath extents and, therefore, may be used to better interpret the underlying transmembrane activity for several relevant *in vitro* and *in vivo* scenarios. The small quantitative differences between the analytical model and the reaction diffusion models are due in part to that fact that the wavefront in the analytical model is assumed to be planar and propagating with uniform conduction velocity while the wavefront in the reaction diffusion bidomain model with an adjacent bath is curved. The front is curved due to the effective lower interstitial resistance at the surface (increased load) where both the amplitude of $V_m(t)$ and $\dot{V}_{m\max}$ are decreased [3] compared to the depth. In

general, the reaction diffusion bidomain solution yields a slightly broader biphasic deflection and slightly increased amplitude due to the transmural electrotonic effects of the bending wavefront. The results also show that the current source model is generally valid for the thick bath case, although the timecourse of the biphasic deflection coincident with activation is narrower than that predicted by either the full bidomain or analytical model, since all the sources are assumed to lie in an infinite volume conductor. The current source model, however, is not valid for the thin and no bath cases.

For tissue with a finite bath extent, the analytical model reveals that the extracellular potential, with a far field reference, can be interpreted of as being composed of the sum of two components; the particular (core-conductor) solution, and the homogeneous solution. The extent of the tissue and bath modulates the contribution these two solutions make to ϕ_e . As the bath becomes infinite, $b \rightarrow \infty$, $H_2(k) \rightarrow 0$, and the solution for ϕ_o and ϕ^h are simplified to the infinite bath derivation of Henriquez *et al.* [1]. As $b \rightarrow a$, the numerator of $H_3(k) \rightarrow 0$ and $\phi^h \rightarrow 0$. The solution for ϕ_e is, thus, the classical core-conductor equation [2]. Potentials from domains with bath thickness between these two extremes have contributions from both the particular and homogeneous solutions. For example, the potential on the tissue surface in the thin bath case (Fig. 2, site 3) is inverted and monophasic as predicted by the particular solution [see (3)] but with a smaller magnitude. This is due to the loading of the bath, through which current may be shunted. When no bath is present, the analytic and numerical solutions both reach the magnitude predicted by the particular solution.

A typical model to compute ϕ_e [see (15)] is based on the assumption that the transmembrane current sources lie in an extensive isotropic bath and, thus, resemble the thick bath case. Note that the impact of the bath depends on the tissue thickness and conductivities, as well as the conductivity of the bath and, therefore, the extensiveness of the bath cannot be determined from knowledge of bath thickness alone [8].

The analytic model is limited by the assumptions that $V_m(z)$ is constant in the depth (i.e., a planar front) and the tissue is equally anisotropic. As shown by Roth, an analogous set of equations can also be derived under the assumption that the intracellular potential is independent of depth (y -direction). This would allow for the tissue to have unequal anisotropy [8]. We expect the two models to have similar predictive power and computational costs.

In summary, the analytical model provides an efficient way to explore the extracellular potential in realistic bidomain preparations that involve a finite bath. In practice, $V_m(z)$ can be obtained from a monodomain model and the analytical model can then be used to estimate the extracellular potentials for tissue with a variably thick bath. The advantage of this approach is that the combined monodomain model and analytical model can be used to accurately solve for extracellular potentials in the presence of ionic inhomogeneities, while using considerably less computational time and resources than an equivalent bidomain.

REFERENCES

- [1] C. Henriquez, N. Trayanova, and Plonsey, "A planar slab bidomain model for cardiac tissue," *Ann. Biomed. Eng.*, vol. 18, pp. 367–376, 1990.
- [2] R. Plonsey, "Action potential sources and their volume conductor fields," *Proc IEEE*, vol. 65, pp. 601–611, 1977.
- [3] C. S. Henriquez, "Simulating the electrical behavior of cardiac tissue using the bidomain model," *Crit. Rev. Biomed. Eng.*, vol. 21, pp. 1–77, 1993.
- [4] M. Spach, W. Miller, E. Miller-Jones, R. Warren, and R. Barr, "Extracellular potentials related to intracellular action potentials during impulse conduction in anisotropic canine cardiac muscle," *Circ. Res.*, vol. 45, pp. 188–204, 1979.

- [5] K. Gima and Y. Rudy, "Ionic current basis of electrocardiographic waveforms: A model study," *Circ. Res.*, vol. 90, pp. 889–96, 2002.
- [6] R. Penland, D. Harrild, and C. Henriquez, "Modeling impulse propagation and extracellular potentials distribution in anisotropic cardiac tissue using a finite volume element discretization," *Comput. Vis. Sci.*, vol. 4, pp. 215–226, 2002.
- [7] C. Luo and Y. Rudy, "A model of the ventricular cardiac action potential: Depolarization, repolarization," *Circ. Res.*, vol. 68, no. 6, pp. 1501–1526, 1991.
- [8] B. J. Roth, "Effect of a perfusing bath on the rate of rise of an action potential propagating through a slab of cardiac tissue," *Ann. Biomed. Eng.*, vol. 24, pp. 639–46, 1996.

Correction of Motion Artifact in Cardiac Optical Mapping Using Image Registration

Gustavo K. Rohde*, Benoit M. Dawant, and Shien-Fong Lin

Abstract—Cardiac motion is one of the main sources of artifacts in epifluorescence imaging experiments. It can cause significant error in electrophysiological measurements such as action potential duration. We present a novel approach that uses image registration based on maximization of mutual information to correct for in-plane cardiac motion in such experiments. The approach is relatively fast (a few seconds per frame) and is performed entirely post acquisition. The image registration approach is an alternative to traditional approaches such as mechanical restraint of the heart or addition of chemical uncouplers. Our results show that the image registration method significantly reduces motion-related artifacts in experimental data.

Index Terms—Image registration, motion correction, mutual information, optical mapping.

I. INTRODUCTION

Optical recording techniques have been widely employed in cardiac electrophysiology for studies of electrodynamics. Optical mapping is based on the proportional change of the induced fluorescence intensity resulting from the change in the transmembrane potentials in dye-stained tissue. The most significant constraint in cardiac optical recording is muscle contraction, which alters the fluorescence intensity and deforms the shape of the optical potentials. When the tissue moves during the recording, its relative location to the sensor and the light source changes, resulting in an artificial variation of fluorescence intensity intermingled with the desired signal. Most significantly, quantification of intensity variation is not meaningful if the fluorescence is recorded from different sites on the tissue in the same recording

Manuscript received September 9, 2003; revised July 2, 2004. This work was supported in part by the National Institutes of Health (NIH) under Grant HL58533. *Asterisk indicates corresponding author.*

*G. K. Rohde is with the Applied Mathematics and Scientific Computation Program, University of Maryland, College Park, MD 20742-4015 USA (e-mail: rohdeg@math.umd.edu).

B. M. Dawant is with the Department of Electrical Engineering and Computer Science, Vanderbilt University, Nashville, TN 37235 USA (e-mail: benoit.dawant@vanderbilt.edu).

S.-F. Lin is with the Division of Cardiology, Department of Medicine, Cedars-Sinai Medical Center, Los Angeles CA 90048 USA and also with the David Geffen School of Medicine, University of California at Los Angeles, Los Angeles CA 90048 USA (e-mail: linsf@cshs.org).

Digital Object Identifier 10.1109/TBME.2004.840464